A Smoothed Eclipse Model for Solar Electric Propulsion Trajectory Optimization

By Jonathan D. Aziz,[1)] Daniel J. Scheeres,[1)] Jeffrey S. Parker,[1)] and Jacob A. Englander[2)]

[1)] *University of Colorado Boulder, USA*
[2)] *NASA Goddard Space Flight Center, USA*

Solar electric propulsion (SEP) is the dominant design option for employing low-thrust propulsion on a space mission. Spacecraft solar arrays power the SEP system but are subject to blackout periods during solar eclipse conditions. Discontinuity in power available to the spacecraft must be accounted for in trajectory optimization, but gradient-based methods require a differentiable power model. This work presents a power model that smooths the eclipse transition from total eclipse to total sunlight with a logistic function. Example trajectories are computed with differential dynamic programming, a second-order gradient-based method.

Key Words: solar electric propulsion, low-thrust trajectory optimization, eclipse, differential dynamic programming

Nomenclature

R	:	radius
$\boldsymbol{r}$	:	position vector
aSR	:	apparent solar radius
aBR	:	apparent body radius
aD	:	apparent distance
$H(x)$	:	Heaviside step function
x^*	:	transition point
γ	:	sunlight fraction
γ_H	:	Heaviside sunlight fraction
$L(x)$	:	logistic function
γ_L	:	logistic sunlight fraction
c_s	:	sharpness coefficient
c_t	:	transition coefficient
P_a	:	power available
P_0	:	reference power level
T_a	:	thrust available
T	:	thrust
I_{sp}	:	specific impulse
g_0	:	gravitational acceleration at sea level
T_{max}	:	maximum thrust
m	:	spacecraft mass
t	:	time
p	:	semi-parameter
f	:	second modified equinoctial element
g	:	third modified equinoctial element
h	:	fourth modified equinoctial element
k	:	fifth modified equinoctial element
L	:	true longitude
E	:	eccentric anomaly
μ	:	gravitational parameter
J_n	:	n-th degree zonal harmonic coefficient
$\boldsymbol{\chi}_p$	:	penumbra apex
α_p	:	penumbra cone angle
$\boldsymbol{s}$	:	solar vector
$\boldsymbol{X}$	:	state vector
τ	:	independent variable of integration
ν	:	true anomaly
$\boldsymbol{f}$	:	transition function

Subscripts

$\odot$	:	Sun
B	:	occulting body
sc	:	spacecraft
$/$	:	*with respect to*
0	:	initial value
f	:	final value
$\oplus$	:	Earth
$\leftmoon$	:	Moon
e	:	penumbra entry or exit

1. Introduction

Low-thrust trajectories about planetary bodies are likely to experience solar eclipses that disrupt the power available to SEP systems. Trajectory optimization without concern for eclipsing is futile when subsequent analysis reveals that a critical maneuver has been placed in the shadow of the central body.

Kéchichian developed analytical expressions for the change in orbital elements due to continuous tangential thrust acceleration over a single revolution with coasting enforced through eclipse.[1)] For changing only the inclination of a circular orbit in presence of Earth shadow, Kéchichian suggests strategies for switching the direction of pure out-of-plane thrust to maximize the inclination change over a single revolution with prescribed eclipse geometry.[2)]

Betts[3)] presents a multi-phase formulations to solve many-revolution geocentric trajectories with eclipsing. First, Betts[3)] constructs an initial guess by stepping through one phase at a time. A control law in each burn phase minimizes the orbit error at shadow entry, which is the end of the burn phase and beginning of a coast phase. The next burn phase resumes at shadow exit. This loosely describes a receding horizon algorithm that continues until the final point is close to the target orbit, after which the trajectory can be refined with a sequential quadratic programming or interior point method.

Graham and Rao[4)] use a collocation method and first solve the minimum time transfer without eclipsing. This nominal trajectory is then evaluated for eclipse passages and is terminated at the first shadow entry. A new nominal trajectory without eclipsing is solved from the shadow exit. Remaining eclipses

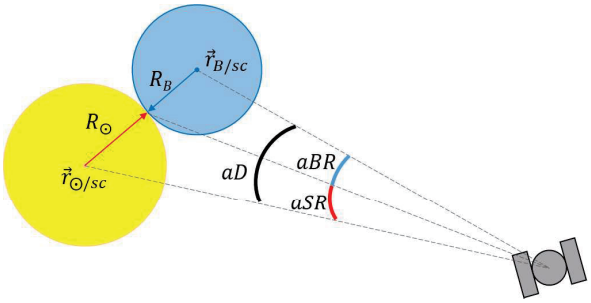

Fig. 1.: Solar and planetary discs as viewed by a spacecraft are on the threshold of an eclipse event. Geometric features relevant to the eclipse model are labeled.

are introduced one at a time in this fashion until the target orbit is reached with all eclipses included.

Ferrier and Epenoy[5] model Earth's shadow as a cylinder and define an auxiliary cylinder just interior or exterior to Earth's shadow. Power available in the shell between the two cylinder radii is chosen as a degree 3 polynomial, but is 0% or 100% otherwise. The polynomial effectively smooths the power available across the eclipse transition, but the model is not differentiable at the switch to or from the polynomial. Nonetheless, transfers from geostationary transfer orbit (GTO) to geosynchronous orbit (GEO) are obtained sequentially with a shooting algorithm, beginning with a null shadow radius that is then increased incrementally to Earth's radius, while each solution becomes the next initial guess.

Advancements in the application of the second-order gradient based-method, differential dynamic programming[8] (DDP), towards spacecraft trajectory optimization have motivated the development of a twice-differentiable power model. This work proposes a model based on the geometry of overlapping discs[6] that smooths the eclipse transition with a logistic function in the same manner that has seen previous success when applied to the discontinuity in discrete number of thrusters available.[7] The proceeding chapters present the mathematical formulation of the smoothed eclipse model and example trajectories computed with an implementation of the Hybrid Differential Dynamic Programming (HDDP) algorithm.[9–11]

2. Eclipse Geometry

By assuming spherical shapes of the Sun and occulting body, and neglecting atmospheric effects, the eclipse geometry can be represented with overlapping circular discs.[6] Figure 1 sketches the eclipse geometry when the edges of the solar disc and occulting body are perceived to be coincident by a spacecraft. Relative position vectors are defined so that

$$\boldsymbol{r}_{\odot/sc} = \boldsymbol{r}_\odot - \boldsymbol{r}_{sc} \tag{1}$$

is the position of the Sun with respect to the spacecraft, and

$$\boldsymbol{r}_{B/sc} = \boldsymbol{r}_B - \boldsymbol{r}_{sc} \tag{2}$$

is the position of the occulting body with respect to the spacecraft. The apparent solar radius and apparent body radius are the angles subtended by their respective radii.

$$aSR = \arcsin\left(\frac{R_\odot}{\|\boldsymbol{r}_{\odot/sc}\|}\right) \tag{3}$$

$$aBR = \arcsin\left(\frac{R_B}{\|\boldsymbol{r}_{B/sc}\|}\right) \tag{4}$$

Lastly, the apparent distance is the angle between the two bodies as viewed by the spacecraft.

$$aD = \arccos\left(\frac{\boldsymbol{r}_{B/sc}\cdot\boldsymbol{r}_{\odot/sc}}{\|\boldsymbol{r}_{B/sc}\|\|\boldsymbol{r}_{\odot/sc}\|}\right) \tag{5}$$

By inspection of Fig. 1, an eclipse occurs when the sum of the apparent radii exceeds the apparent distance between the two bodies,

$$aSR + aBR > aD\,. \tag{6}$$

If the inequality holds, then $aSR \leqslant aBR$ indicates a total eclipse, and $aSR > aBR$ indicates a partial eclipse. The partial eclipse is an annular eclipse when the spacecraft is in the occulting body's antumbra. These conditions also assume that $\boldsymbol{r}_{B/sc} < \boldsymbol{r}_{\odot/sc}$.

3. Smoothed Sunlight Fraction

The sunlight fraction is a discontinuous function of the geometry of the spacecraft, Sun, and occulting body positions,

$$\gamma = \begin{cases} 0, & aSR + aBR > aD \text{ and } aSR \leqslant aBR \\ (0,1), & aSR + aBR > aD \text{ and } aSR > aBR\,, \\ 1, & aSR + aBR \leqslant aD \end{cases} \tag{7}$$

where the total eclipse occurs in umbra, and the intermediate case is itself a discontinuous function that depends on if the spacecraft is in penumbra or antumbra. Additional relations from the overlapping disc geometry allow for the computation of the sunlight fraction in each of these cases.[6] However, the smoothed eclipse model imposes a zero-thrust constraint for both partial and total eclipse. The sunlight fraction is then a step function between 100% and 0%, and relies only on Eqs. (3) to (5) for the necessary geometry. With the Heaviside definition of a step function, the sunlight fraction is half-valued at the eclipse transition.

$$H(x) = \begin{cases} 0, & x < x^* \\ 0.5, & x = x^* \\ 1, & x > x^* \end{cases} \tag{8}$$

$$\gamma_H = \begin{cases} 0, & aSR + aBR > aD \\ 0.5, & aSR + aBR = aD \\ 1, & aSR + aBR < aD \end{cases} \tag{9}$$

Eq. (8) is the unit Heaviside step function that transitions at x^*, and is applied to the eclipse transition to develop the Heaviside sunlight fraction in Eq. (9). The Heaviside step function alone does not resolve the issue of a discontinuous power model, but it can be approximated by a logistic function with smooth derivatives that are favorable for gradient-based optimization.

$$L(x) = \frac{1}{1 + \exp[-c_s(x - x^*)]} \tag{10}$$

$$\gamma_L = \frac{1}{1 + \exp\{-c_s[aD - c_t(aSR + aBR)]\}} \tag{11}$$

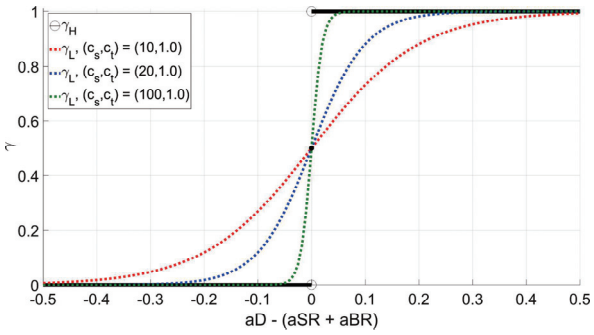

Fig. 2.: The sunlight fraction is represented by a Heaviside step function and logistic functions of different sharpness coefficients.

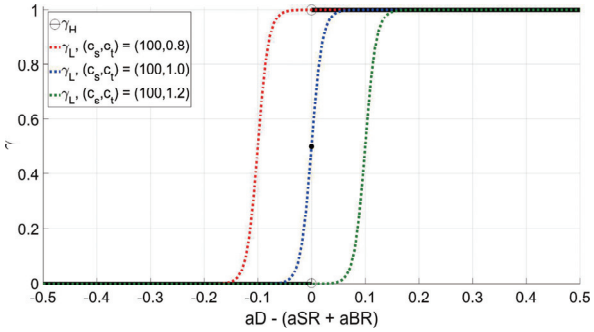

Fig. 3.: The sunlight fraction is represented by a Heaviside step function and logistic functions with different transition coefficients.

Eq. (10) is the unit logistic function that is a smooth approximation to the unit Heaviside step function. Eq. (11) is the logistic sunlight fraction and constitutes the smoothed eclipse model.

Figures 2 and 3 depict the Heaviside sunlight fraction and the logistic sunlight fraction for different (c_s, c_t) values. Sharpness coefficient c_s determines the slope of the curve at the transition point. Transition coefficient c_t scales the total angle of the apparent solar and body radii, and effectively moves the transition point.

Selection of a (c_s, c_t) pair might be driven by numerical behavior, desired model accuracy, or mission operations. An intermediate c_s value that is not too steep or flat is likely to benefit optimizer performance, but at the expense of model accuracy. When model accuracy is a priority, the (c_s, c_t) pair that minimizes the smoothed model error could be selected. Further improvements could be gained by considering (c_s, c_t) as functions of time or orbital radius, for example, in lieu of constant values, to reflect the changing eclipse geometry during a transfer. From a mission operations perspective, it might be necessary to power down/up the spacecraft at a certain rate and offset from eclipse entry/exit. That rate and offset are prescribed by (c_s, c_t) in the smoothed eclipse model.

4. Trajectory Optimization Example

Transfers from low Earth orbit (LEO) to GEO characteristically encounter frequent solar eclipses. That rate is expectedly once per revolution in the early stages of the trajectory, but possibly declining with changes to the orbital altitude and inclination. To demonstrate the utility of the smoothed eclipse model, the minimum-fuel LEO to GEO transfer from Betts[3] is reproduced with HDDP as the optimization method.

Table 1.: Spacecraft Parameters.

m_0	1000 kg	T_{max}	1.445 N
I_{sp}	1849.347748 s	P_0	13.103192 kW

Table 2.: Initial and Target Orbit States.

p_0	6878.14 km	p_f	42241.095482 km
f_0	0.0	f_f	0.0
g_0	0.0	g_f	0.0
h_0	-0.253967	h_f	0.0
k_0	0.0	k_f	0.0
L_0	π		
t_0	0.0		

4.1. Constant Power With Smoothed Eclipsing

Power available to the spacecraft is modeled by scaling a reference power level by the logistic sunlight fraction.

$$P_a = \gamma_L P_0 \tag{12}$$

Higher-fidelity modeling is possible by replacing P_0 with improved power models, such as inverse-square decay with heliocentric distance, or a polynomial. It is assumed that the spacecraft has gimbaled solar arrays and/or gimbaled thrusters so that the arrays are always wholly effective. Thrust available from the SEP system is then,

$$T_a = \frac{2P_a}{I_{sp} g_0}, \tag{13}$$

and often scaled by a duty cycle or engine efficiency. Ref. 3) considers $T_a = T_{max}$ for burn phases, so T_{max} is used to set P_0 for this example. Table 1 lists the necessary spacecraft parameters.

Selection of a (c_s, c_t) pair began by choosing $c_t = 1.0$ so that there is no shift in the eclipse transition. A value of $c_s = 289.78$ was found to minimize the error between the smoothed and discontinuous eclipse model for a range of orbital radii and eccentricities. In fact, it was found that the Sun and body radii and Sun-body distance drive the optimal c_s value, rather than the spacecraft's planetocentric orbit. For example, $c_s \approx 289.78$ was obtained for geocentric orbits, but the same procedure found $c_s \approx 432.35$ appropriate for Mars-centered orbits.

4.2. Boundary Conditions and Dynamics

Initial conditions for a 500 km altitude LEO with 28.5° inclination are stated in terms of the modified equinoctial elements in Table 2. The target GEO is also listed with the exception of the unconstrained true longitude. Dynamics include solar and lunar third body perturbations, and perturbations from Earth zonal harmonics J_2, J_3, and J_4. Dynamic model parameters are summarized in Table 3. The Sun's position, velocity, and acceleration are obtained from heliocentric Keplerian motion of the Earth beginning with the osculating orbital elements for the Earth at the reference epoch. The Moon's state is similarly obtained by geocentric Keplerian motion.

Betts selects the true longitude as the independent variable and arrives at an optimal final mass of $m_f = 718.79$ kg in $L_f = 248.5$ revolutions. For this example, the eccentric anomaly is

Table 3.: Dynamic Model Parameters.

$\mu_\oplus$	398600.436380 km^3/s^2	J_2	1.082639×10^{-3}
$\mu_\odot$	132712440018 km^3/s^2	J_3	-2.565×10^{-6}
$\mu_\leftmoon$	4902.798815 km^3/s^2	J_4	-1.608×10^{-6}
$R_\oplus$	6378.14 km	g_0	9.80665×10^{-3} km/s^2
$R_\odot$	695500 km	(c_s, c_t)	(289.78, 1.0)
Reference Epoch	2457377.5 Julian Date TDB		

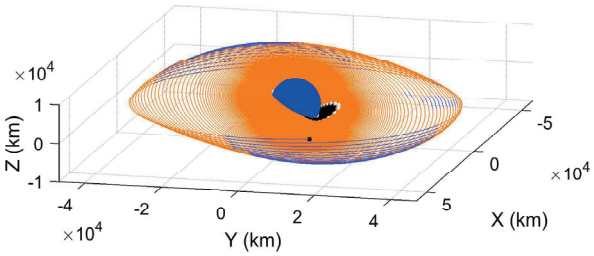

Fig. 4.: The trajectory computed by HDDP with the smoothed eclipse model active is shown in a three-dimensional view. Thrust arcs are colored orange and coast arcs in sunlight are colored blue. Eclipse arcs are colored on grayscale from black for total eclipse to white for total sunlight. A square marker indicates the end of the transfer.

chosen as the independent variable and the endpoint is fixed at $E_f = 248.5$ revolutions. The trajectory is integrated with a fixed-step fifth-order Dormand-Prince method[12] at a discretization of 60 stages per revolution. An initial guess considers $T = 0$ for all stages so that HDDP iteration begins from a ballistic trajectory through 248.5 revolutions in LEO.

Results were generated on an Intel Xeon E5-2680 v3 2.50 GHz CPU with 128 GB memory and Red Hat Enterprise Linux 7 operating system. State transition matrices and tensors were computed in parallel across 12 cores with OpenMP.[13]

4.3. Initial Results

The LEO to GEO trajectory computed by HDDP with the smoothed eclipse model active is shown in Figure 4, and the eclipse passages are higlighted in Figure 5. An improved final mass of $m_f = 733.29$ kg is obtained in a time of flight $t_f = 45.78$ days. True longitude accumulates to 249.1 revolutions. This result is listed alongside other trials in Table 4. Computational performance is summarized in Table 5.

Eclipse passages interfere with initial thrusting to raise the orbital radius from LEO. Coast arcs in sunlight are driven by the minimum propellant objective and do not occur until late in the transfer. A terminal coast arc is included in the revolution count and indicates that the target orbit states are met before the prescribed number of revolutions.

5. Penumbra Terminator Detection

Eclipse effects are most accurately included in the numerical integration of spacecraft trajectories if integration steps fall exactly on the penumbra terminator. While the smoothed eclipse model benefits from an automatic response in power available during eclipse without the need for event detection, a fixed mesh of integration stages will step over the eclipse entry and exit points. The spacecraft effectively sees prolonged sunlight into penumbra entry and prolonged eclipse through penumbra exit. The discretization error is illustrated in Figure 5, where penumbra entry and exit locations have been marked on an equatorial projection of the initial trajectory result. There are several ways to fix this error. One is to use a variable time-step integrator. Another is to compensate analytically, which is discussed in the proceeding sections.

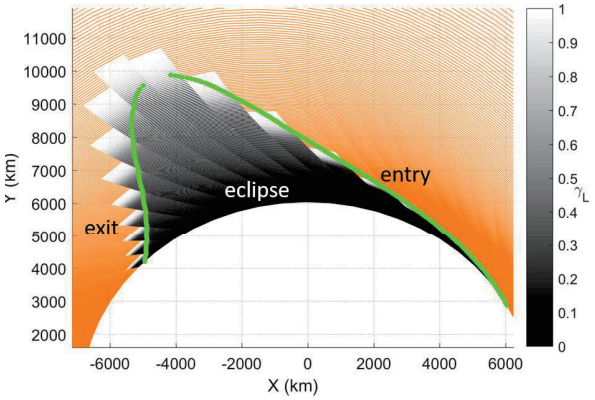

Fig. 5.: An equatorial projection of the eclipse passages is shown with penumbra entry and exit locations marked.

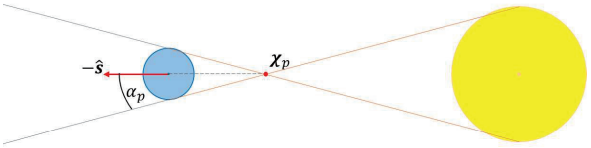

Fig. 6.: Geometry of the penumbral cone.

5.1. Calculation Method for Penumbra Entry and Exit

Penumbra entry and exit locations can be estimated as the intersection of the line between two integration stages and the penumbral cone. Calculations in this study do not correct for light-time but capture the instantaneous penumbral cone geometry that is illustrated in Figure 6.

The origin of the penumbral cone is a function of the solar and occulting body radii and the solar vector.

$$\boldsymbol{\chi}_p = \frac{R_B}{R_B + R_\odot}\boldsymbol{s} \tag{14}$$

Note that $\boldsymbol{s} = \boldsymbol{r}_{\odot/B}$. The penumbral cone axis is represented by a unit vector opposite the solar vector, $-\hat{\boldsymbol{s}}$. The penumbral cone angle is

$$\alpha_p = \sin^{-1}\left(\frac{R_B}{\|\boldsymbol{\chi}_p\|}\right). \tag{15}$$

A spacecraft with position vector $\boldsymbol{r}$ is within the penumbral cone if the vector difference $\boldsymbol{r} - \boldsymbol{\chi}_p$ forms an angle with the cone axis that is smaller than the cone angle.

$$-(\boldsymbol{r} - \boldsymbol{\chi}_p)^T\hat{\boldsymbol{s}} \geqslant \|(\boldsymbol{r} - \boldsymbol{\chi}_p)\| \cos\alpha_p \tag{16}$$

Squaring Eq. (16) yields a quadratic inequality with roots along the penumbra terminator.

$$(\boldsymbol{r} - \boldsymbol{\chi}_p)^T(\hat{\boldsymbol{s}}\hat{\boldsymbol{s}}^T - I\cos^2\alpha_p)(\boldsymbol{r} - \boldsymbol{\chi}_p) \geqslant 0 \tag{17}$$

Consider the position vectors $\boldsymbol{r}_1$ and $\boldsymbol{r}_2$ just before and after penumbra entry. Inserting the line $\boldsymbol{r}(t) = \boldsymbol{r}_1 + t\boldsymbol{r}_2$ into Eq. (17) and solving for the roots of $at^2 + 2bt + c = 0$ provides the points

of intersection of $\boldsymbol{r}(t)$ and the penumbral cone. After defining $M = (\hat{\boldsymbol{s}}\hat{\boldsymbol{s}}^T - I\cos^2\alpha_p)$, the coefficients are

$$a = \boldsymbol{r}_2{}^T M \boldsymbol{r}_2 \tag{18a}$$

$$b = \boldsymbol{r}_2{}^T M(\boldsymbol{r}_1 - \boldsymbol{\chi}_p) \tag{18b}$$

$$c = (\boldsymbol{r}_1 - \boldsymbol{\chi}_p)^T M(\boldsymbol{r}_1 - \boldsymbol{\chi}_p). \tag{18c}$$

The smaller root $t = (-b \pm \sqrt{b^2 - ac})/a$ estimates the spacecraft penumbra entry, while the larger root extends the line to the far side of the penumbral cone. For position vectors $\boldsymbol{r}_1$ and $\boldsymbol{r}_2$ just before and after penumbra exit, a positive root estimates the spacecraft penumbra exit and a negative root is the far side intersection.

5.2. Mesh Adjustment for Penumbra Entry and Exit

The method for calculation of penumbra entry and exit points can be leveraged for mesh adjustment to place integration stages on the penumbra terminator. First, a generic integration step relies on the current state and the step size.

$$\boldsymbol{X}_2 = \boldsymbol{f}(\boldsymbol{X}_1, \tau_2 - \tau_1) \tag{19}$$

State vector $\boldsymbol{X}$ includes the position vector $\boldsymbol{r}$ or orbital elements that determine $\boldsymbol{r}$, while $\boldsymbol{f}$ is a transition function, e.g., the integral of the equations of motion, and τ is the independent variable of integration.

Given $\boldsymbol{r}_1$ and having computed $\boldsymbol{r}_2$, the two positions can be checked for a change in eclipse conditions. The step size $\tau_2 - \tau_1$ should be selected so that the penumbra will not be stepped over entirely. If eclipse entry or exit is detected, the estimated intersection of the trajectory and penumbra terminator is $\boldsymbol{r}_e = \boldsymbol{r}(t_e)$ where t_e is selected as the appropriate root obtained by Eqs. (17) and (18). The angle between $\boldsymbol{r}_1$ and $\boldsymbol{r}_e$ is the approximate change in true anomaly to reach the penumbra terminator.

$$\Delta\nu = \cos^{-1}\left(\frac{\boldsymbol{r}_e{}^T \boldsymbol{r}_1}{\|\boldsymbol{r}_e\|\|\boldsymbol{r}_1\|}\right) \tag{20}$$

Then the independent variable at the terminator $\tau_e = \tau(\boldsymbol{X}_1, \tau_1, \Delta\nu)$ can be determined, and two consecutive steps replace Eq. (19).

$$\boldsymbol{X}_e = \boldsymbol{f}(\boldsymbol{X}_1, \tau_e - \tau_1) \tag{21a}$$

$$\boldsymbol{X}_2 = \boldsymbol{f}(\boldsymbol{X}_e, \tau_2 - \tau_e) \tag{21b}$$

As an approximation, $\boldsymbol{r}_e$ targets the penumbra terminator but is expected to err on either side. Stepping too far provides a conservative model of the power available, so it may be worthwhile to further increment $\Delta\nu$. This is perhaps a more realistic representation of a spacecraft shutting down early and remaining down for a time after an eclipse event. In the worst case, a single-step integrator carries the incorrect power available from $\boldsymbol{r}_e$ to $\boldsymbol{r}_2$. Multi-step methods, however, should have integration sub-steps on the correct side of the penumbra terminator to offset this error.

6. Results with Penumbra Detection

Accuracy of the initial result is improved by inserting stages at the penumbra entry and exit locations detected by the methods of Section **5.** HDDP is restarted with the previous solution as an initial guess. Power available is again computed with the smoothed eclipse model but stages for eclipse passages are forced to coast by setting $T_{max} = 0$. For each revolution with an eclipse, the new throttle constraint is assigned for the inserted penumbra entry stage and subsequent stages up to but not including the inserted penumbra exit. While the improved trajectory is similar, its penumbra entry and exit locations correspond to the previous solution. Subsequent iterations insert stages to update the penumbra entry and exit locations to further improve solution accuracy. The new trajectory is practically indistinguishable aside from the improved resolution at the penumbra terminator. Color contours of the logistic sunlight fraction are not used in Figure 8 (as they were in Figure 4). As the smoothed model is active, stages adjacent to the penumbra see γ_L less than but approximately 100%.

Table 4.: Trajectory Optimization Results.

Iteration	m_f (kg)	t_f (days)
1	733.29	45.78
2	732.61	45.58
3	732.41	45.51
4	732.29	45.49
5	732.24	45.46
Betts[3)]	718.79	43.13

Table 5.: Computational Performance.

Iteration	HDDP Iterations	Runtime (sec)
1	161	9362
2	60	3758
3	39	2398
4	31	1978
5	18	1181

Thrust steering profiles are depicted in Figure 7. The in-plane thrust angle is measured from the transverse direction about the angular momentum, and the out-of-plane thrust is measured from the orbit plane about the radial direction. The thrust magnitude profile confirms the expected bang-bang control, though initial coast arcs are owed to eclipsing, while later coast arcs are for propellant savings. Steering angles indicate how initial steering is devoted to raising the orbital radius. The out-of-plane component increases throughout the transfer as it becomes more fuel efficient to change the inclination at a larger orbital radius.

7. Conclusion

A smoothed eclipse model has been presented for use in computing optimal trajectories for space missions that employ solar electric propulsion. The logistic sunlight fraction is introduced as the visible sunlight through the smoothed eclipse transition from total eclipse (and vice versa) to total sunlight by a logistic function. The model is continuously differentiable and suitable for gradient based optimization methods. As a percentage of the sunlight available, the smoothed eclipse model is a coefficient that can be paired with arbitrary power models. A set of tuning parameters allows for mission designers to adjust the rate at which power available to the spacecraft declines or recovers, and to shift the location of the eclipse discontinuity. An example trajectory computed with HDDP and the smoothed eclipse model improves upon the mass delivered for a LEO to GEO trajectory in the literature. A refined solution corrects for dis-

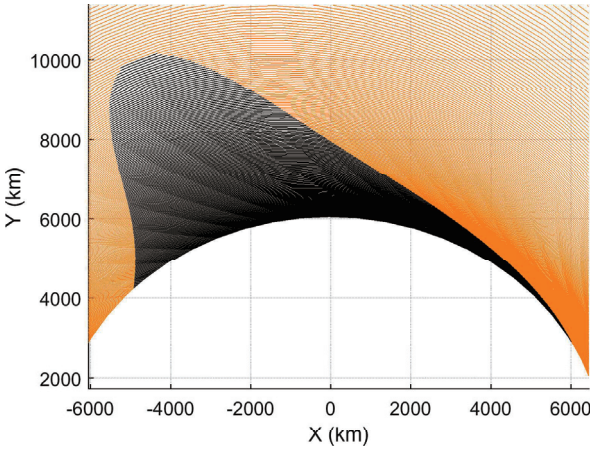

Fig. 9.: An equatorial projection of the eclipse passages is shown for the final trajectory with penumbra detection.

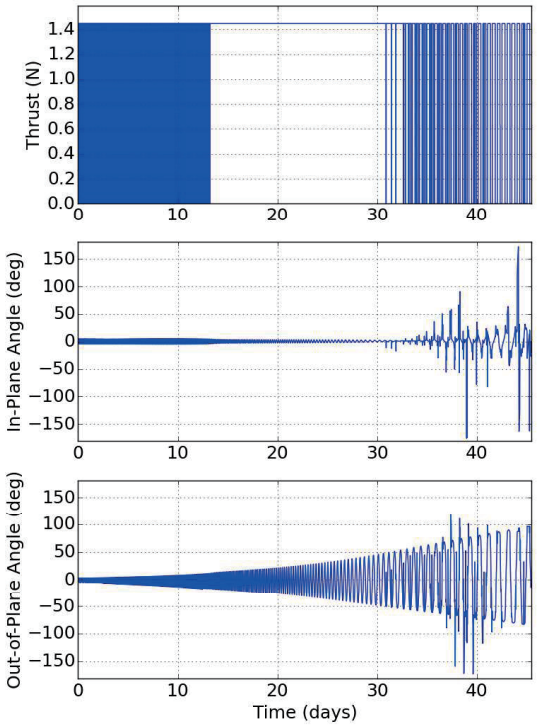

Fig. 7.: Thrust magnitude, in-plane, and out-of-plane thrust angles are shown for the duration of the transfer.

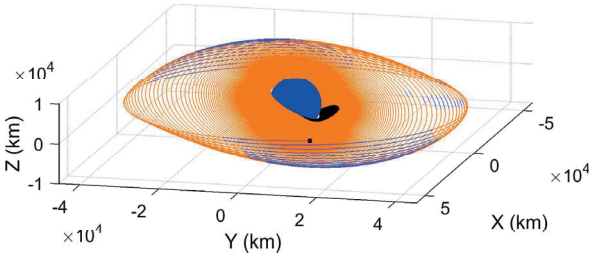

Fig. 8.: The final trajectory with penumbra detection is shown in a three-dimensional view. Thrust arcs are colored orange, coast arcs in sunlight are colored blue, and eclipse arcs are colored black. A square marker indicates the end of the transfer.

cretization errors by inserting penumbra entry and exit locations with only a minor adjustment to the delivered mass.

Acknowledgments

This work was supported by a NASA Space Technology Research Fellowship. This work utilized the Summit supercomputer, which is supported by the National Science Foundation (awards ACI-1532235 and ACI-1532236), the University of Colorado Boulder, and Colorado State University. The Summit supercomputer is a joint effort of the University of Colorado Boulder and Colorado State University.

References

1) Kéchichian, J.A.: Orbit Raising with Low-Thrust Tangential Acceleration in Presence of Earth Shadow. *Journal of Spacecraft and Rockets*, **35** (1998), pp. 516-525.
2) Kéchichian, J.A.: Low-Thrust Inclination Control in Presence of Earth Shadow. *Journal of Spacecraft and Rockets*, **35** (1998), pp. 526-532.
3) Betts, J.T.: Optimal Low Thrust Orbit Transfers With Eclipsing, *Optimal Control Applications and Methods*, **36** (2014).
4) Graham, L.F. and Rao, A.V.: Minimum-Time Trajectory Optimization of Low-Thrust Earth-Orbit Transfers with Eclipsing, *Journal of Spacecraft and Rockets*, **53** (2016), pp. 289-303.
5) Ferrier, C.H. and Epenoy, R.: Optimal Control for Engines with Electro-Ionic Propulsion Under Constraint of Eclipse, *Acta Astronautica*, **48** (2001), pp. 181-192.
6) Montenbruck, O. and Gill, E.: *Satellite Orbits, Models, Methods and Applications*, Springer, 2005.
7) Englander, J.A., Vavrina, M.A. and Hinckley, D.: Global Optimization of Low-Thrust Interplanetary Trajectories Subject to Operational Constraints, AAS/AIAA Space Flight Mechanics Meeting, Napa, CA, February, 2016.
8) Jacobson, D.H. and Mayne, D.Q.: *Differential Dynamic Programming*, American Elsevier Publishing Company, Inc., 1970.
9) Lantoine, G. and Russell, R.P.: A Hybrid Differential Dynamic Programming Algorithm for Constrained Optimal Control Problems, Part 1: Theory, *Journal of Optimization Theory and Applications*, **154** (2012), pp. 382-417.
10) Lantoine, G. and Russell, R.P.: A Hybrid Differential Dynamic Programming Algorithm for Constrained Optimal Control Problems, Part 2: Application, *Journal of Optimization Theory and Applications*, **154** (2012), pp. 418-442.
11) Aziz, J.D., Parker, J.S., Scheeres, D.J., and Englander, J.A.: Low-Thrust Many-Revolution Trajectory Optimization via Differential Dynamic Programming and a Sundman Transformation, AAS/AIAA Space Flight Mechanics Meeting, San Antonio, TX, February, 2017.
12) Prince, P. and Dormand, J.: High order embedded Runge-Kutta formulae, *Journal of Computational and Applied Mathematics*, **7** (1981), pp. 67-75.
13) O.A.R. Board: OpenMP Application Program Interface Version 3.0, (2008).